Applied Surface Science 698 (2025) 163031

Contents lists available at ScienceDirect

Applied Surface Science

journal homepage: www.elsevier.com/locate/apsusc

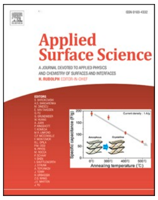

Full Length Article

Green steel at atomistic scale: Ab initio simulation of surface reduction mechanism of Wüstite (FeO) by hydrogen

Chunhe Jiang [a,b], Kejiang Li [a,*], Jianliang Zhang [a,c,*], Yan Ma [d,e]

[a] School of Metallurgical and Ecological Engineering, University of Science and Technology Beijing, Beijing 100083, China
[b] Technical Support Center for Prevention and Control of Disastrous Accidents in Metal Smelting, University of Science and Technology Beijing, Beijing 100083, China
[c] School of Chemical Engineering, The University of Queensland, St Lucia, QLD 4072, Australia
[d] Max-Planck-Institute for Sustainable Materials, Max-Planck-Straße 1, Düsseldorf 40237, Germany
[e] Department of Materials Science and Engineering, Delft University of Technology, Mekelweg 2, 2628 CD Delft, the Netherlands

ARTICLE INFO

Keywords:
Green steel
Ab initio molecular dynamic
Meta-dynamics
Redox reaction
Reaction pathway
Energy barrier

ABSTRACT

The reduction of FeO (wüstite) to Fe represents the final and slowest step in the hydrogen-based direct reduction of iron ores for sustainable ironmaking. However, the atomistic-scale mechanisms and kinetics of this process remain poorly understood. Here, we employ *ab initio* meta-dynamics simulations to investigate reaction pathways and energy barriers for this redox process on FeO(1 0 0) and FeO(1 1 1)$_{\text{O-terminated}}$ surfaces. Differences in surface configurations lead to variations in the number of H_2 molecules required, reaction pathways, and energy barriers. The FeO surface exhibits an autocatalytic effect, facilitating H_2 dissociation and reducing the energy barrier for breaking H_2 molecular bonds. Nevertheless, hydrogen dissociation and adsorption, forming O–H bonds, constitute the primary rate-limiting step. Following this, the Fe-O bond spontaneously breaks in the presence of individual H atoms. Increasing H_2 partial pressure enhances reaction efficiency by raising the density of reactive H_2 molecules, consistent with macroscopic observations. These insights advance the atomistic-scale understanding of hydrogen-based direct reduction, highlighting the influence of pressure and rate-limiting factors.

1. Introduction

Steel, an alloy predominantly composed of iron and carbon, is the most widely utilized metallic material globally. For over 3,000 years, it has provided essential strength, durability, and longevity to components across construction, infrastructure, transportation, appliances, machinery, and more, all at a relatively low cost[1]. With an annual production of 1.9 billion tons, steel far surpasses the production volume of any other metallic material. The second most produced metal, aluminum, reaches approximately 100 million tons per year, emphasizing the critical role of steel in supporting human civilization and enhancing quality of life. However, the steel industry faces today a pressing challenge in decarbonization, as it accounts for approximately 8 % of global annual CO_2 emissions[2,3]. Current CO_2 emissions average 1.8–2.0 tons per ton of steel produced[4]. Notably, 70–80 % of these emissions originate from the conventional ironmaking process, which relies on the blast furnace–oxygen converter route. This method uses coal and coke as reducing agents, resulting in significant CO_2 generation as a by-product[5]. In contrast, hydrogen can be used as a promising alternative reductant to fossil carbon, featuring an endothermic reaction pathway and producing only water as a by-product. Consequently, hydrogen-based reduction technologies are viewed as a potentially sustainable and environmentally friendly alternative for ironmaking, provided the hydrogen is sourced from renewable energy[6–8].

Currently, hydrogen is explored as a (co–)reductant in three different types of ironmaking processes: blast furnace[9], direct reduction[10], and plasma smelting reduction [11]. The blast furnace relies on coke, which serves multiple critical functions: it provides a porous column structure that facilitates gas transport, ensuring the furnace's counter-current reactor properties and mechanical stability. The majority of coke is consumed for heating while simultaneously generating reductant gas. This occurs initially through its reaction with hot oxygen to form CO_2, which is then converted into CO reductant gas via the Boudouard reaction. The CO subsequently reacts with solid iron ore to reduce it.

---

* Corresponding authors at: School of Metallurgical and Ecological Engineering, University of Science and Technology Beijing, Beijing 100083, China (K. Li and J. Zhang).

E-mail addresses: likejiang@ustb.edu.cn (K. Li), jl.zhang@ustb.edu.cn (J. Zhang).

https://doi.org/10.1016/j.apsusc.2025.163031
Received 17 February 2025; Received in revised form 12 March 2025; Accepted 19 March 2025

Additionally, coke in direct contact with iron oxides acts as a reducing agent via direct reduction reactions. This multifaceted role of coke—-providing porosity, structural stability, heat, and reductant production—presents significant challenges for fully substituting it with hydrogen in the blast furnace process. An alternative is hydrogen plasma smelting reduction, which has demonstrated practical feasibility and efficiency in reducing iron oxides, even at partial H_2 pressures as low as 10 % or lower. However, the scalability of this process for industrial applications remains a challenge due to limited large-scale trials. A key issue is the non-linear scalability of plasma-based processes, necessitating detailed upscaling experiments with progressively larger reactors. These trials must address critical aspects such as electrode design and materials, refractory materials, and slag metallurgy to ensure the process's viability and efficiency at industrial scales[12–14]. Direct reduction with hydrogen as a reductant is another alternative: hydrogen gas and hydrogen containing gas mixtures have long been investigated as a primary reducing agent in direct reduction processes, with direct reduction furnaces demonstrating industrial scalability in terms of both size and production volume[6,13,15–18]. As a result, direct reduction is considered the most viable technology for industrial implementation using fully green hydrogen as the reductant. Pilot-scale hydrogen-based direct reduction (HyDR) plants, such as the HYBRIT[19] project and the tkH_2steel[20] project, have already been established, showcasing the potential for large-scale adoption.

In the HyDR process, the reduction of iron oxides strongly depends on pressure[21,22] and temperature[23,24]. At temperature above 570 °C, iron oxide is reduced to iron through a stepwise reduction: Fe_2O_3 (hematite) → Fe_3O_4 (magnetite) → FeO (wüstite) → Fe. At temperatures below 570 °C, the equilibrium shifts in a way that does not favor the stability of FeO[25]. The reduction then proceeds via $Fe_2O_3 \rightarrow Fe_3O_4 \rightarrow$ Fe. The HyDR is a complex gas–solid reduction process, where several studies have addressed and in part elucidated the influence of various microstructure, feedstock, and processing factors on process performance, efficiency and metal yield. Ma *et al.*[17] have categorized the reaction behaviors into three distinct scales: macroscopic, mesoscopic, and micro-to-atomic-scale behaviors. The Ellingham energy balance for redox processes between different oxides paired with different reductants shows that H_2-based reduction of iron oxides is, in principle, feasible. However, a significant thermodynamic disparity exists between reduction by carbon-based reductants and hydrogen. While the reduction of iron oxides with CO is exothermic, the reduction with H_2 is endothermic. Consequently, H_2-based reduction processes require additional energy input through co-fueling and higher operating temperatures to sustain reactor operation[26,27]. From a kinetic perspective, the solid-state direct reduction rate via H_2 is significantly higher than that with CO as reductant[28,29], approximately 2.5 times. The influencing effects of specific process parameters, such as temperature [29,30], pressure[31], and gas composition[32,33], on the direct reduction process remain active areas of investigation. Mesoscopic scale mean-field analysis is frequently employed to elucidate phenomena in HyDR, including phase transitions, porosity evolution, and mass transfer [18,34,35]. Studies suggest that the initial porosity of mineral phases facilitates H_2 percolation and, crucially, the removal of H_2O[36,37]. As the reaction progresses, the outbound migration of oxygen atoms increasingly constrains the overall reduction rate. In the final stages, during the transition from wüstite to iron, the formation of a dense iron layer on the outer shell of the pellets significantly hinders the migration of residual oxygen, thereby limiting reaction kinetics[38]. Thus, the reduction of FeO to Fe has been confirmed as the rate-limiting step in direct reduction[39–41].

The mechanistic pathways of FeO reduced by H_2, pivotal to this transition, are complex and multifaceted. Experimental efforts to elucidate these mechanisms have been hindered by the high temperatures and rapid reaction kinetics characteristic of the process. As a result, a detailed understanding of the stepwise reaction sequence and the associated energy barriers remains incomplete. This brings atomistic simulations into the play, as an alternative means for a more detailed probing of the underlying reduction mechanisms and kinetics. However, studying the reduction process at the atomistic scale using ab initio molecular dynamics (AIMD) simulations over a limited timeframe, such as 100 ps, presents significant challenges. Rare events, including H–H bond dissociation, H atom adsorption on the FeO surface, and O–Fe bond breaking, occur infrequently in AIMD simulations and reactive molecular dynamics (MD) simulations due to the constrained simulation timescale. To accurately capture these phenomena, the integration of enhanced sampling techniques, such as meta-dynamics, is essential. Uddin *et al.*[42] applied reactive force field molecular dynamics (ReaxFF-MD) in combination with meta-dynamics to compute the free energy changes associated with the dissolution of Ca ions from various Ca_3SiO_5 surfaces. Similarly, Li *et al.*[43] employed AIMD coupled with meta-dynamics using the PLUMED software to investigate the dissolution process of tricalcium silicate in water, effectively elucidating the surface reaction pathways. In contrast, no comparable studies have been conducted on the reduction of iron oxides.

Therefore, in this study, we investigate the atomistic reduction mechanism of FeO by H_2 using ab initio meta-dynamics simulations. The reduction process of FeO with different crystallographic orientations by H_2 is analyzed and compared to elucidate the underlying reaction pathways, free energy changes, energy barriers, and microstructural characteristics. Our findings reveal that H_2 dissociation involves significant energy barriers, making it a critical rate-limiting step in the early precursor stages of the reduction process. Upon adsorption of a hydrogen atom onto an oxygen atom, forming a hydroxyl bond, the strength of the original O–Fe bond is substantially weakened, leading to a marked propensity for its dissociation. We also observed that the intermediate adsorption structures during the reduction process aligned with the IR spectra of various microstructures obtained in redox experiments involving FeO and H_2[44,45]. These findings offer profound new insights into the mechanism of O atom removal from the FeO surface during hydrogen reduction.

2. Methods

2.1. Atomistic model

For the FeO model, a 2 × 2 × 3 supercell was constructed, and the bottom 2-layer set of the atoms remained fixed. Then, a 10Å thick vacuum layer was placed above the FeO surface. Both the FeO(1 0 0)–H_2 and FeO(1 1 1)$_{\text{O-terminated}}$-H_2 models consist of 100 atoms, as shown in Fig.1(a) and Fig.1(b), with a lattice parameters of 8.66Å×8.66Å×20.83Å and 10.61Å×12.25Å×16.25Å, respectively.

2.2. Ab initio meta-dynamics simulations

All calculations are conducted using the QuickStep package of CP2K [46,47]. The electronic structure is characterized using the Kohn-Sham density functional theory approach. The implementation of density functional theory (DFT) is grounded in the Gaussian and plane wave framework. Molecular orbitals for valence electrons are depicted using Goedecker-Teter-Hutter (GTH) pseudopotentials[48,49]. The wave function was expanded on a double-ζ valence polarized (DZVP)[50] basis set. The energy cutoff and REL_CUTOFF were set to 500 Ry and 50 Ry, respectively. The exchange–correlation effects were described using the Perdew-Burke-Ernzerhof (PBE) functional[51], complemented by the application of Grimme's D3 dispersion correction for enhanced accuracy[52]. In the simulation, the nuclei were modeled under the Born-Oppenheimer approximation, employing a time step of 0.5 fs. All simulations were conducted at 1173 K to mirror industrial reactor conditions through the use of a Nose-Hoover thermostat [53], which was coupled to the system with a time constant of 1000 fs within the NVT ensemble. The convergence criterion for the energy was established at 10^{-11} Hartree for precision.

In density functional theory, incorporating a Hubbard-type U potential correction term mitigates certain limitations of the local and semi-local exchange–correlation functionals while maintaining computational efficiency. Nonetheless, the effectiveness of the DFT + U approach is highly contingent upon the selection of appropriate Hubbard U values[54]. Conventional DFT tends to underestimate the Coulomb repulsion among the localized 3d electrons in iron[55,56]. To address this limitation, the DFT + U method has been employed to achieve a more accurate depiction of these electronic states[57,58]. This semi-empirical approach introduces an additional potential specifically for the 3d states of iron, enhancing the reliability of the calculations. The equations of state of FeO with different + U value is shown in **Fig.S1**. The most stable lattice constant of our simulation is in the range of 4.27–4.32Å, which is closer to the experimental value[59]. Therefore, the + U value does not obviously affect the equations of state of FeO. The value of the band gap increased monotonically with the increscent + U value, as shown in **Fig.S2**. When the + U value assumes a value of 1 eV or 2 eV, respectively, there is no band gap of wüstite. In the existing literature[60–64], the theoretical values for the band gap of wüstite vary between 1.5 and 2.4 eV. To ensure that the energy bands remain within a reasonable range while minimizing the impact of + U on the simulations, we selected a U value of 4 eV, with a band gap of 1.74 eV.

Meta-dynamics not only explores the system's potential energy surface—capturing the enthalpic contributions as a function of collective variables (CVs)—but also estimates the occurrence probabilities of various conformations or states through statistical sampling, indirectly reflecting entropic contributions. By examining the free energy minima of the system, the chemical reaction pathway can be effectively determined. During chemical reactions, atomic configurations evolve, with the formation of O–H bonds and the breaking of O-Fe bonds altering the local coordination environment of oxygen. Consequently, the coordination number (CN) of oxygen was chosen as the collective variable in the simulation. Specifically, CN(O-Fe) represents the coordination number of a target oxygen ion with its neighboring iron ions in the FeO crystals, while CN(O–H) denotes the coordination number of the target oxygen ion with hydrogen ions that stem from the H_2 molecules. The coordination number (CN) is defined using the PLUMED code formalism as follows[65,66]:

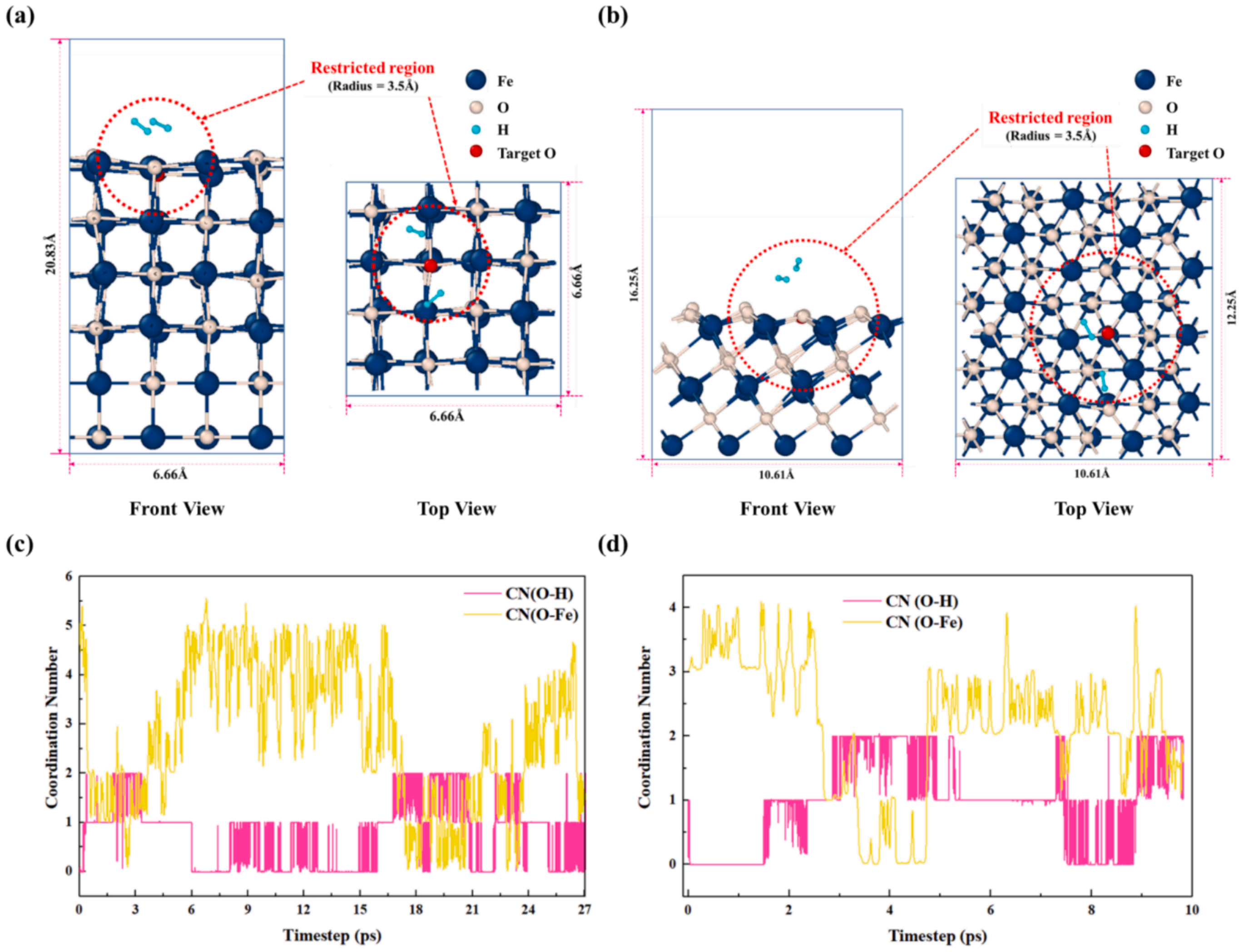

Fig. 1. Setup of the simulation model and the evolution of collective variable in the metadynamics simulations. CN: Coordination number. (a) The reaction surface of the FeO crystal is (1 0 0), and the target oxygen atom is coordinated with 5 Fe atoms. (b) The reaction surface of FeO crystal is (1 1 1)-$O_{terminated,}$ and the target oxygen atom is coordinated with 3 Fe atoms. (c) The evolution of the CN(O-Fe) and CN(O–H) in the FeO(1 0 0)–H_2 model. (d) The evolution of the CN(O-Fe) and CN (O–H) in the FeO(1 1 1)O-terminated-H_2 model. (The mazarine, white, and cyan spheres are Fe, O, and H atoms, respectively. The red sphere represents the target O atom for collective variable calculation. The "restricted region" is the region in which the H_2 molecules are allowed to move freely in meta-dynamics simulation, and this effectively increases the frequency of contact between H_2 and the FeO interface.). (For interpretation of the references to colour in this figure legend, the reader is referred to the web version of this article.)

$$CN(O,X)=\sum_{j\in X}s_{ij}(r_{ij})=\sum_{j\in X}\frac{1-\left(\frac{r_{ij}-d_0}{r_0}\right)^4}{1-\left(\frac{r_{ij}-d_0}{r_0}\right)^{10}},X=Fe\ or\ H \tag{1}$$

where, r_{ij} represents the distance between atoms i and j. The term $s_{ij}(r_{ij})$ is a rational type switching function that characterizes the coordination between atoms i and j. The parameter d_0 is the central value of this function, while r_0 denotes the acceptance distance for the switching function, at which the function will be n/m at $d_0 + r_0$. In our definition, d_0 is set to 2.2 and 1.05, corresponding to the equilibrium bond length between the O-Fe atoms and O–H atoms, respectively. The value of r_0 is chosen as 0.65 and 0.2, approximating half of the full width at half maximum of the radial distribution function for O-Fe and O–H, respectively.

Gaussian hills were added at intervals of every 20 timesteps, each with an initial height of 2.5 kJ/mol and a width of 0.1 for both CVs. The simulations employed a bias factor of 30. The time evolution of CV(CN (O-Fe)) and CV(CN(O–H)), which are detailed in the Fig. 1**(c)** and Fig. 1 **(d)**.

2.3. Structural analysis and spectroscopy calculations

Radial distribution functions (RDFs) were employed to analyze the short-range order and long-range disorder within the systems, enabling the correlation of local atomic structures with macroscopic properties. Representing the probability of locating an ion at a position r within a distance Δr from a specified reference ion, the RDFs (g_{ij}) are expressed as:

$$g_{ij}(r)=\frac{V}{N_iN_j}\sum_{j}\frac{\langle n_{ij}(r-\Delta r/2,r+\Delta r/2)\rangle}{4\pi r^2\Delta r} \tag{2}$$

where N_i represents the total number of atomic species i present in the system, V the volume, $n_{ij}(r-\Delta r/2, r+\Delta r/2)$ the average number of ions j surrounding the ion i within a distance $r \pm \Delta r/2$. In addition to determining the local order, RDFs also provide basic structural information.

To study the vibrational spectra during the reaction process between FeO and H_2, we selected the structure of H_2 adsorbed on the FeO surface for IR spectrum analysis. The structure with adsorbed H atoms was computed and examined using the *Vibrational_Analysis* module of the *Quickstep* package in CP2K, maintaining consistency with the parameters used in the *ab initio* meta-dynamics simulations. Vibrational bands were calculated with CP2K, which provides reliable predictions for the wavenumbers and intensities of the fundamental, overtone, and combination bands. The second derivative of the Hamiltonian was determined using the harmonic approximation equation in the *Multiwfn* formalism[67], enabling accurate calculation of the infrared frequencies.

3. Results

3.1. Determination of the reaction model

The reduction process of Fe_2O_3 proceeds in a stepwise manner, with the final step, the conversion of wüstite (FeO) to metallic iron (Fe), serving as the critical rate-limiting stage. In situ X-ray diffraction experiments investigating the reduction of Fe_2O_3 by H_2, it was observed that the FeO(1 0 0) surface, a characteristic reconstructed surface facet, readily forms during the reduction of hematite[38]. Hence, it has been chosen as one of the reference facet models for the reaction simulation. Since the outer facet surface atoms of the FeO(1 1 1) surface are all unsaturated oxygen atoms, the FeO(1 1 1)$_{\text{O-terminated}}$ surface exhibits a higher adsorption energy for H_2[68]. Therefore, the FeO(1 1 1)$_{\text{O-terminated}}$ surface has also been selected for comparative analysis. Since our simulation study focuses on the reaction pathways and energy changes associated with oxygen movement and removal from the crystal surface, only two H_2 molecules were included in the simulation to eliminate partial pressure as an additional parameter. To accelerate the reaction rate and optimize computational efficiency, an external potential was applied to confine two H_2 molecules within fixed spherical regions centered on the target oxygen atom, as shown in Fig. 1**(a)** and Fig. 1**(b)**. The motion area is a spherical region with a radius of 3.5Å centered on the target oxygen atom. The specific confining potential is defined by the equation:

$$V(r)=A\left(\frac{r}{R}\right)^8, r=\sqrt{(X-a)^2+(Y-b)^2+(Z-c)^2} \tag{3}$$

Here, A = 1 eV is the strength coefficient, R = 3.5Å is the characteristic radius, and the center coordinates (a,b,c) define the spatial position of the potential. This potential is applied exclusively to hydrogen atoms, ensuring no direct influence on other regions of the system. The confining potential introduces an additional energy term for the controlled atoms. Due to its high-order power-law form (r^8), the potential remains negligible for $r < R$ but increases significantly for $r > R$, effectively restricting the atoms from moving far from the central region. This design minimizes perturbations to the internal equilibrium configurations of the system, preserving the energetics of the core region while achieving the desired spatial confinement.

3.2. Reduction path of FeO(1 0 0) by H_2

The 2-dimensional free energy surface of the FeO(1 0 0)–H_2 system is shown in Fig. 2**(a).** The coordinate of the state is presented in the form of X(CN(O-Fe), CN(O–H)), in which X indicates the label on the free energy surface. The energy variations within the rectangular region visible in Fig. 2**(a)** are attributed to lattice vibrations, an effect amplified by the bias forces inherent in the meta-dynamics simulation methodology. During the simulation, these bias forces can induce the artificial formation of unconventional structures. For instance, the elongation or breaking of the O-Fe bond in the absence of H_2 adsorption is highly unlikely to occur under normal conditions.

The results suggested that the O removal most likely underwent two stages: the adsorption of the first H atom and the bond-breaking process of three O-Fe bonds, see A(5,0) → E(2,1) in Fig. 2**(a)**, and the adsorption of the second H atom and the breaking process of the remaining O-Fe bonds, see E(2,1) → H(0,2) in Fig. 2**(a)**. The first stage has only one pathway: First, an O atom with a CN(O-Fe) of 5 adsorbs one hydrogen atom, followed by a gradual decrease in CN(O-Fe) to 2, which is the process from A(5,0) → B(5,1) → C(4,1) → D(3,1) → E(2,1) in Fig. 2**(a)**. Based on the free energy surface, three reaction pathways are suggested. Parth I: E(2,1) → F(1,1) → G(1,2) → H(0,2); Parth II: E(2,1) → I(2,2) → G (1,2) → H(0,2); Parth III: E(2,1) → F(1,1) → J(0,1) → H(0,2). The details of independent reaction paths will be discussed in the following sections.

Fig. 2**(b)** shows the changes in free energy, and Fig. 3 presents the corresponding possible reaction configuration in the FeO(1 0 0)–H_2 model. The adsorption of H_2 onto the FeO surface is a complex process that necessitates continuous interaction between the H_2 molecule and the surface atoms. When the H_2 molecule interacts concurrently with both oxygen and iron atoms on the surface, its molecular bond dissociates, resulting in the formation of the structure B(5,1). As shown in Fig. 2 **(b)**, the energy increases by 1.03 eV. Subsequently, the structure unit B spontaneously breaks the O-Fe bond, undergoing the B(5,1) → C(4,1) → D(3,1) → E(2,1) process sequence, with associated energy barriers of 0.15, 0.19, and 0.03 eV, respectively. As the configurational free energy decreases progressively, this reaction process can proceed spontaneously. Among the observed configurations, apart from the initial structure, configuration E(2,1), where the target O atom is bonded to 2 Fe atoms and 1H atom, is the most stable configuration in the reaction process, and it is also the final state of the first stage.

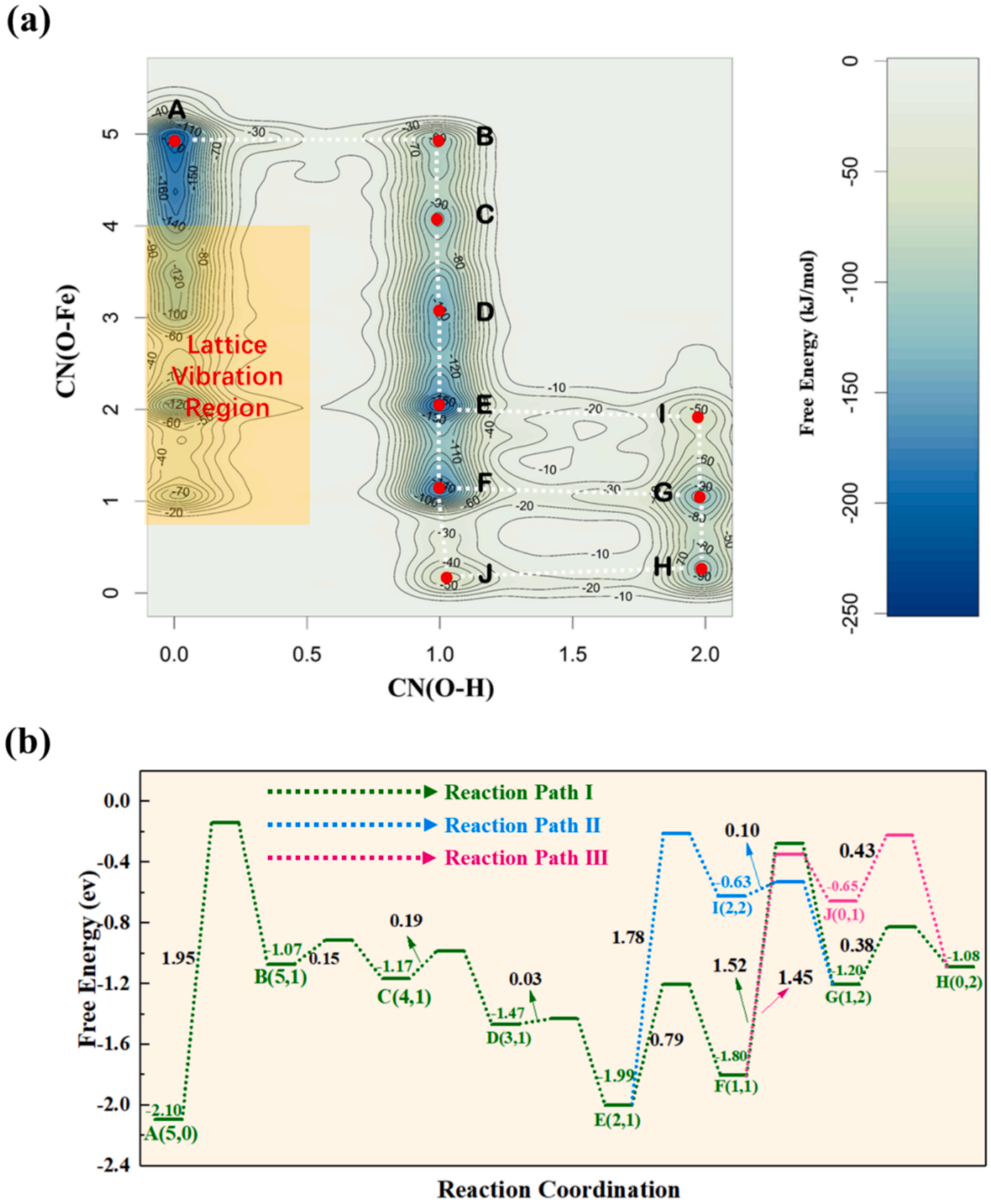

Fig. 2. The possible reaction mechanism of the FeO(1 0 0)–H_2 model. (a) The two-dimensional free energy surface landscape with variables of CN(O–H) and CN(O-Fe). (The crystal vibration region refers to the physical structure that is far from its normal expected state due to the system bias during the free energy surface filling process. It is a necessary methodological condition because the filling process of certain structures may undergo an evolution for these kinds of structures.). (b) The evolution of free energy with different reaction pathways. (The (x,y) represents the coordination state, x is the CN(O-Fe), and y is the CN(O–H). The top number of (x, y) is the free energy of a specific structure. Different colors mean different reaction pathways, corresponding to microstructure evolution.).

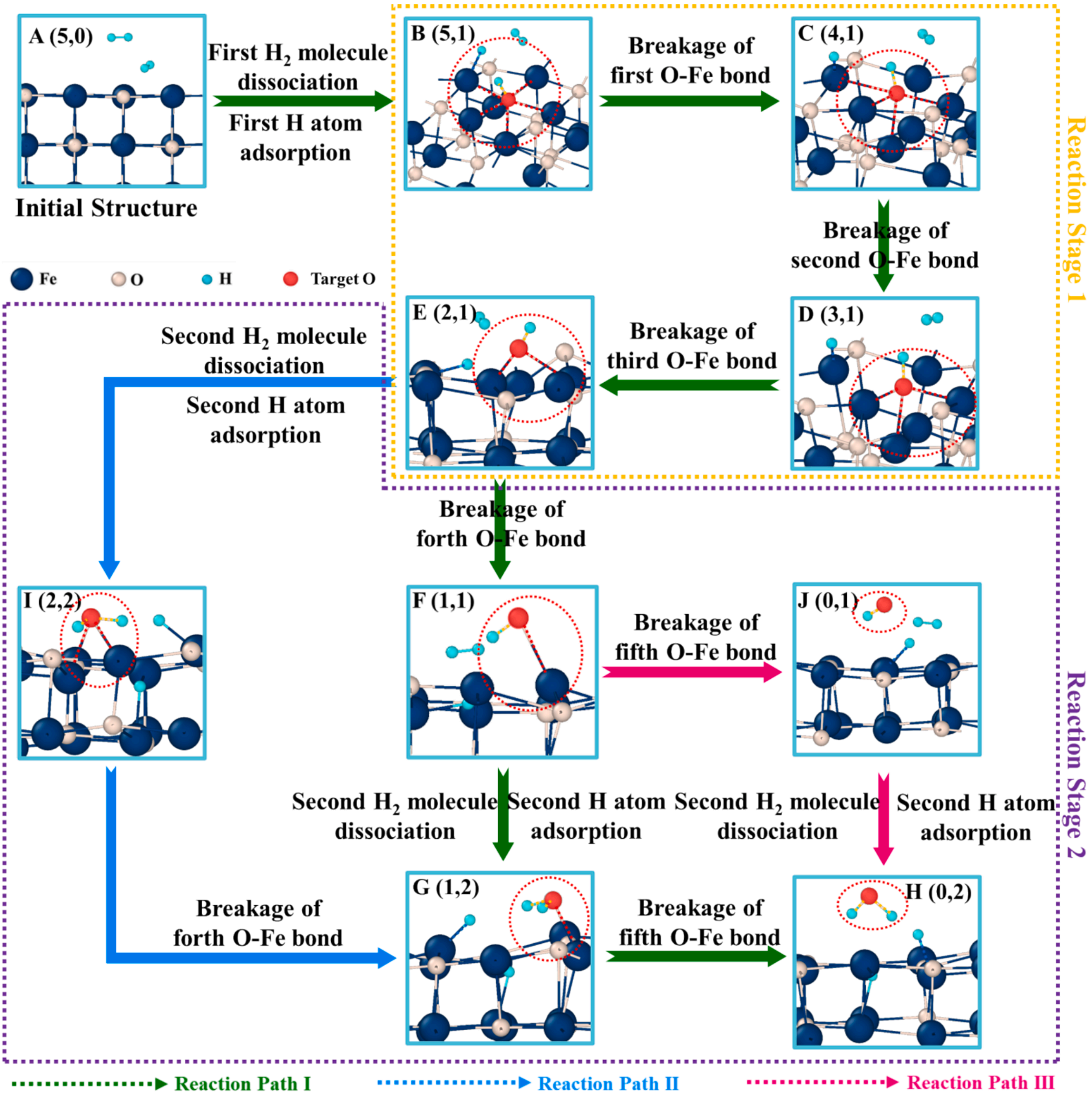

Fig. 3. The microstructure evolution corresponds to different reaction pathways (The mazarine, white, and cyan spheres are Fe, O, and H atoms, respectively). The red sphere represents the target O atom for collective variable calculation. The black number represents the reaction energy barrier). (For interpretation of the references to colour in this figure legend, the reader is referred to the web version of this article.)

Structure E(2,1) is the starting point for the second stage reaction, as shown in Fig. 3. Three possible reaction pathways can be analyzed from the change in free energy. The green line represents the first possible reaction pathway. Under the influence of H atoms, the O atom continues to break the O-Fe bond, eventually forming a state with CN(O-Fe) of 1, see structure F(1,1) in Fig. 3. The free energy change for this step increases, indicating that the reaction is endothermic and non-spontaneous. Nevertheless, the energy barrier is relatively low assuming a value of 0.79 eV, suggesting that the step is kinetically favorable. Subsequently, upon interaction with an additional H_2 molecule, the second H_2 undergoes dissociation. This process is analogous to the dissociation of the first H_2 molecule in the initial stage, requiring the overcoming of a significant energy barrier of 1.52 eV and similarly representing an endothermic reaction.

The dissociation of H_2 molecules is also a rate-limiting step. One hydrogen atom continues to adsorb with the oxygen atom, while the other hydrogen atom bonds with an iron atom, forming the structure G (1,2) in Fig. 3. A single hydrogen atom is observed to occupy the position initially held by an oxygen atom in the FeO crystal structure. This hydrogen atom interacts with neighboring oxygen and iron atoms, contributing to the structural stability. Subsequently, through the combined action of two hydrogen atoms, an H_2O molecule detaches from the original crystal structure, forming the H(0,2) configuration depicted in Fig. 3. For the continued formation of H_2O molecules, the involvement of a second H_2 molecule is required. The trajectory of two hydrogen molecules is illustrated in **supplementary Fig.S3**. The corresponding reduction process can be viewed in the supplementary video.

The blue line represents the second possible reaction pathway. In this pathway, the second H_2 molecule dissociates under the influence of configuration E(2,1), producing two separate hydrogen atoms. One hydrogen atom interacts with an oxygen atom, increasing its coordination CN (O–H) to 2, while the other hydrogen atom bonds with an iron atom, analogous to the H_2 dissociation in the first reaction pathway. Similarly, one hydrogen atom occupies the position initially held by an oxygen atom in the crystal lattice, as the oxygen atom adsorbs the two hydrogen atoms and migrates above the original crystal surface. Since this step involves the dissociation of H_2, it is evident that the energy barrier for the E(2,1) → I(2,2) step is relatively high, 1.78 eV, and the process is strongly endothermic, with an energy change of up to 1.36 eV. Structure I(2,2) is relatively unstable and can spontaneously break one of the O-Fe bonds with a low energy barrier of only 0.10 eV, resulting in the formation of structure G(1,2). The subsequent steps involving H_2O formation and removal align with those described in the first reaction pathway.

The purple line represents a third possible reaction pathway. In this pathway, structure F(1,1) undergoes further O-Fe bond breaking facilitated by a single hydrogen atom, leading to the formation of a free –OH group. This step has a relatively high associated energy barrier of 1.52 eV and is thus strongly endothermic. Subsequently, an additional H_2 molecule interacts with the FeO structure, resulting in the adsorption of two hydrogen atoms on the surface. The free –OH group then reacts with one of these hydrogen atoms to form an H_2O molecule. This subsequent step is relatively facile and exothermic.

3.3. *Reduction path of FeO(1 1 1)$_{\text{O-terminated}}$ by H_2*

For the FeO(1 1 1)$_{\text{o-terminated}}$ model, it has also been validated that the structure with CN(O-Fe) = 3 and CN(O–H) = 0 is the most stable under the FeO(1 1 1)$_{\text{o-terminated}}$ system, as shown in Fig. 4**(a)**. There is free energy filling for structures with CN(O-Fe) = 3 and CN(O–H) = 2. The CN variation curve in Fig. 1**(d)** shows that the filling in this region mainly occurred after the formation of H_2O. Moreover, this structure does not appear continuously but re-emerged under the influence of the meta-dynamics bias from the final structure. Additionally, by comparing this with the free energy of structure C(2,1), the direct transformation from structure B(3,1) to structure C(2,1) is the most probable and most accessible pathway. In general, substances preferentially follow reaction pathways that require lower activation energy and are thus kinetically or thermodynamically more favorable. Therefore, the free energy in the region with CN(O-Fe) = 3 and CN(O–H) = 2 has not been included in the further scope of the analysis for this reaction pathway.

Fig. 4**(b)** and Fig. 5 show the free energy variations and corresponding structural evolution under different reaction pathways, respectively. In this reaction model, the reaction behavior can also be divided into two stages. The first stage is mainly the transformation from structure A(3,0) into structure C(2,1). Initially, the hydrogen molecule dissociates under the influence of the oxygen atoms on the FeO surface, forming two hydrogen atoms adsorbed on the oxygen atoms, as shown in structure B(3,1). This process exhibits a relatively high energy barrier of 1.38 eV but necessitates the absorption of only 0.19 eV of thermal energy. Subsequently, structure B(3,1) spontaneously breaks an O-Fe bond, forming structure C(2,1). At this point, the energy barrier is very small, accompanied by an exothermic reaction of 0.71 eV. Structure C (2,1) represents the global free energy minimum point, that is, the most stable structure.

The second stage also encompasses three possible reaction pathways, with the structure of CN(O-Fe) = 2 and CN(O–H) = 1 serving as the initial state of the reaction. The green line represents the first possible reaction pathway, where structure C(2,1) undergoes a strong endothermic process, breaking an O-Fe bond. The energy barrier at this stage is 1.84 eV (the highest energy barrier compared with the other reaction steps) in the first possible pathway, indicating that it acts as the rate-limiting step for this pathway variant. Subsequently, another hydrogen atom adsorbed on an oxygen atom combines with the target oxygen atom, increasing the coordination CN(O–H) to 2, resulting in structure E(1,2). This step is a mildly exothermic process, associated with a moderate energy barrier of 0.58 eV. Subsequently, under the influence of two hydrogen atoms, the final O-Fe bond breaks spontaneously, releasing 0.69 eV of energy. A single H_2 molecule is sufficient to complete the formation of an H_2O molecule.

The blue line represents the second possible reaction pathway. Here, a hydrogen atom adsorbed onto another oxygen atom and migrates to the target oxygen atom, forming two O–H bonds (structure G(2,2)). This step requires a global maximum energy barrier of 1.90 eV, the highest energy barrier compared with the other reaction steps in the second possible pathway. Structure C(2,1) represents the global energy minimum point, signifying it as the most stable structure. Altering this structure thus generally necessitates overcoming a significant energy barrier. However, in the presence of two hydrogen atoms, the remaining two O–Fe bonds spontaneously break, resulting in the exothermic formation of an H_2O molecule.

The purple line represents the third possible reaction pathway. After undergoing the C(2,1) → D(1,1) transition, identical to the first possible pathway, the final O-Fe bond breaks under the influence of a hydrogen atom, leading to the formation of structure H(0,1). This reaction step is endothermic, with an energy barrier of 0.59 eV. Following this, the –OH group reacts with a hydrogen atom adsorbed on the FeO surface, leading to the formation of an H_2O molecule. Across all three possible pathways, the reaction involves only a single H_2 molecule, a distinct mechanism compared to the FeO(1 0 0) surface. This highlights fundamentally different rate-limiting principles between the two surface configurations.

3.4. *Structural and IR spectroscopy analysis*

Infrared (IR) spectroscopy is a powerful tool for characterizing specific aspects of the nano- and microstructural evolution associated with the reaction processes discussed above. It thereby can serve as a valuable metric for bridging theoretical predictions with experimental observations. The IR spectroscopy of the H_2 and FeO reaction model is simulated and shown in Fig. 6**(a)**. First, it can be clearly observed that there is a band between 860–950 cm^{-1}, which is a response to the vibration of the FeO crystal structure. Secondly, there is a noticeable band in the range of 294–736 cm^{-1}, which corresponds to the H-Fe-O–H structure. A spectral band corresponding to the Fe-H structure is observed in the range of 1440–1620 cm^{-1}. Additionally, a sharp peak appears around 3000 cm^{-1}, resembling the IR spectrum characteristic of the OH functional group in organic compounds[44]. All peak positions identified in the IR spectroscopy align with experimentally measured bands, indicating that the simulation results are in agreement with the experimental findings [45].

Further, Fig. 6**(b), (c), and (d)** represent the radial distribution function for H-H, Fe-H, and O–H, respectively. The bond lengths between atoms can be directly evaluated using the RDF. For the H-H bond, the RDFs in both models are nearly identical, indicating a bond length of 0.75 Å, consistent with the known H_2 bond length[69]. In contrast, the Fe-H bond lengths differ significantly between the two models, measuring 1.95 Å and 2.75 Å, respectively. This suggests that the former represents a bonded state, while the latter corresponds to a non-bonded interaction, indicating whether the Fe atom is actively involved in the reaction process. Regarding the O–H bond, both models exhibit consistent bond lengths of 0.95 Å, aligning with the bond length found in water molecules[70].

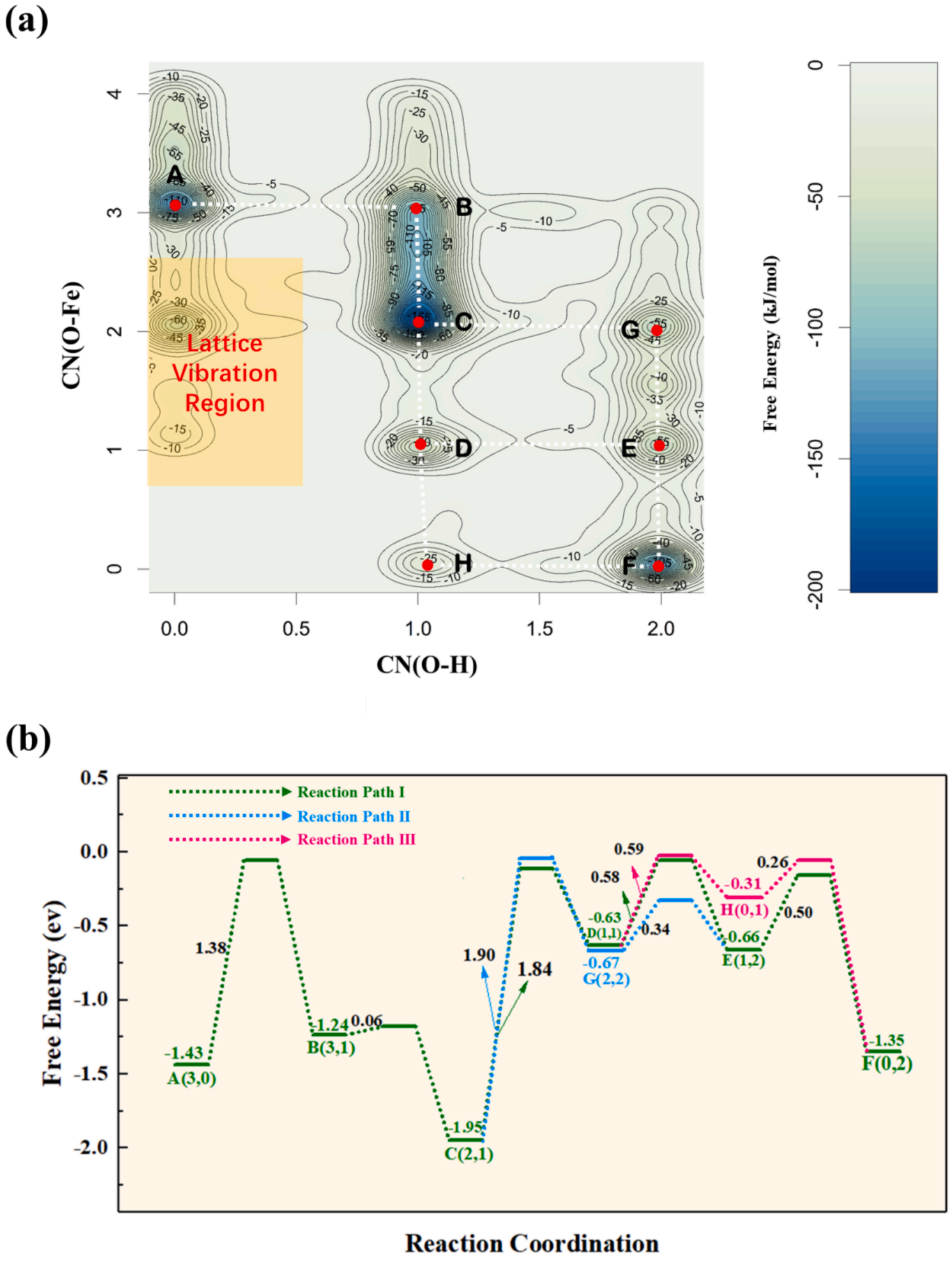

Fig. 4. The possible reaction mechanisms with the FeO(111-O)–H_2 model. (a) The two-dimensional free energy surface landscape with variables of CN(O–H) and CN (O-Fe). (The crystal vibration region refers to the physical structure that is far from its normal expected state due to the system bias during the free energy surface filling process. It is a necessary methodological condition because the filling process of certain structures may undergo an evolution for these kinds of structures.) (b) The evolution of free energy with different reaction pathways. The (x,y) represents the coordination state, x is the CN(O-Fe) and y is the CN(O–H). The top number of (x,y) is the free energy of a specific structure. Different colors mean different reaction pathways, corresponding to microstructure evolution.).

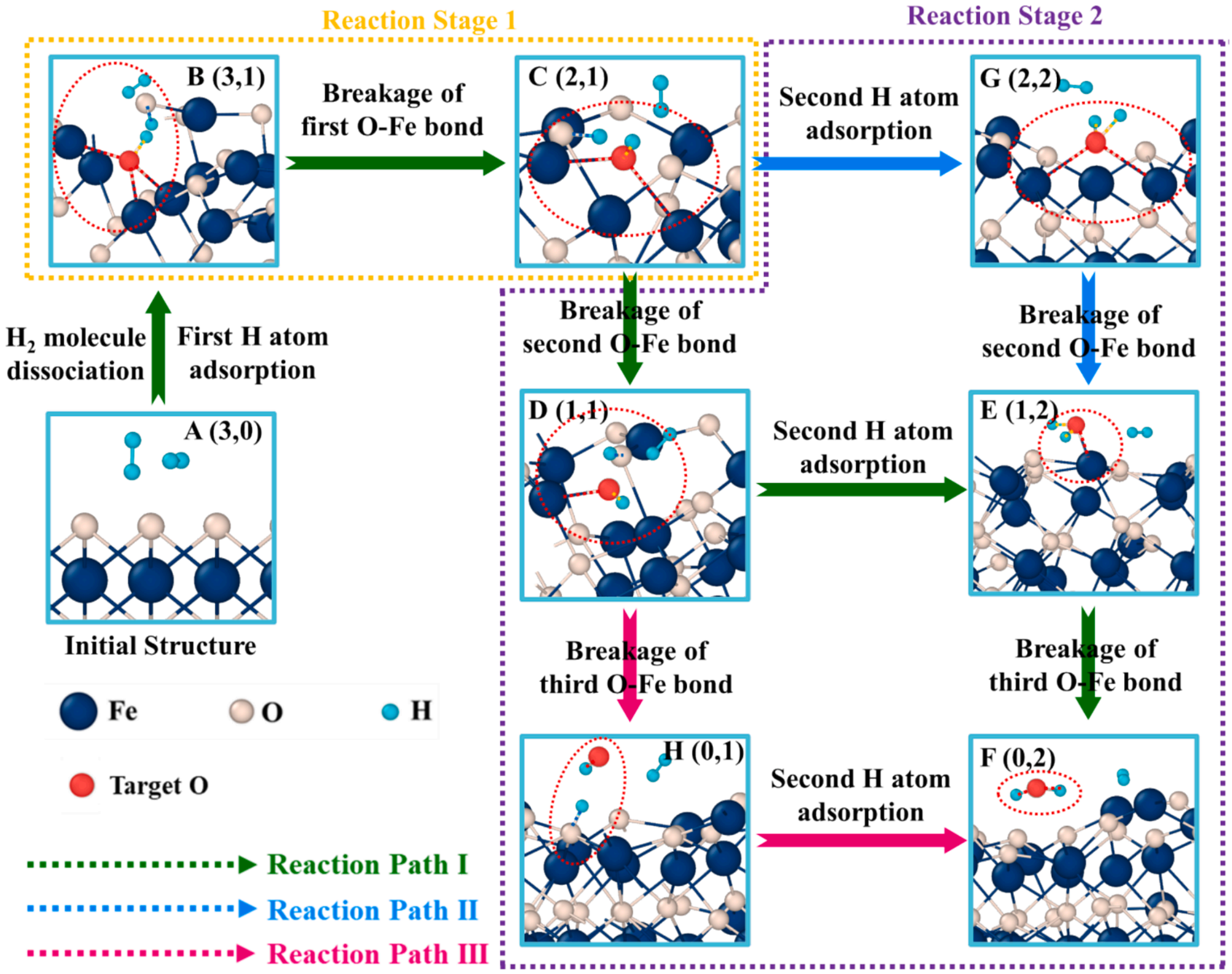

Fig. 5. The specific microstructure evolution depends on the respective reaction pathways. (The mazarine, white and cyan spheres are Fe, O and H atoms, respectively. The red sphere represents the target O atom for collective variable calculation. The black number refers to the reaction energy barrier.). (For interpretation of the references to colour in this figure legend, the reader is referred to the web version of this article.)

4. Discussion

The reaction pathways for H_2 to reduce oxygen atoms from FeO surfaces vary significantly depending on the crystal orientation, as evidenced by differences in free energy profiles and energy barriers. In the FeO(1 0 0)-H_2 model, pathways I and II, illustrated in the supporting video, represent continuous reaction processes, as depicted in Fig. 3. Pathway III, on the other hand, is a reaction sequence leading to intermediate structures that are captured while filling the free energy surface, reflecting steps that are otherwise unlikely to occur in a continuous reaction process. Pathways I and II should be the expected energetically favorable reduction reaction pathways. Free energy analysis indicates that pathway III is a feasible reaction pathway, with the transient independent existence of free OH groups as a potential intermediate. Notably, the participation of two H_2 molecules is essential for the formation of H_2O molecules. Furthermore, due to the interaction between Fe atoms and H atoms, the H atoms adsorbed onto Fe atoms are unable to migrate to O atoms. The cleavage of H_2 is a high-energy barrier process and serves as the rate-limiting step. However, the dissociation of H_2 on FeO also exhibits a catalytic effect, demonstrating that FeO promotes H_2 dissociation. It is well-established that the bond energy of H_2 is 4.46 eV. In our study, both the energy barrier and the free energy change associated with this process are significantly lower than this value. The reaction steps involving changes in the coordination number (CN) of O–H encompass two key processes: H_2 dissociation and H atom adsorption. Zhang et al.[59] had reported already that the adsorption of H atoms on the FeO(1 1 1)$_{\text{O-terminated}}$ surface releases more energy, which explains why the endothermic process in the first step of the FeO (1 1 1)$_{\text{O-terminated}}$ model is smaller. Therefore, it can be inferred that when H_2 comes into contact with the FeO(1 0 0) surface, increasing the amount of H_2 has a positive effect on promoting the overall reaction.

In the FeO(1 1 1)$_{\text{O-terminated}}$ model, the reduction reaction occurs in two stages, involving two high-energy barrier steps, as illustrated in Fig. 5. The energy barrier of the first step is notably lower than that of the FeO(1 0 0) model, indicating a superior catalytic performance. Furthermore, the overall heat consumption is reduced. In the first stage, the rate-limiting step is also governed by the dissociation of H_2. Notably, in this model, a single H_2 molecule is sufficient to complete the formation of one H_2O molecule. The rate-limiting step in the second stage is fundamentally distinct. It involves the disruption of the stable C(2,1) structure, identified as the globally most stable configuration. Since materials naturally tend toward the lowest-energy state, overcoming the stability of this structure requires surmounting a significant energy barrier. Subsequent reaction steps following the breakdown of the C

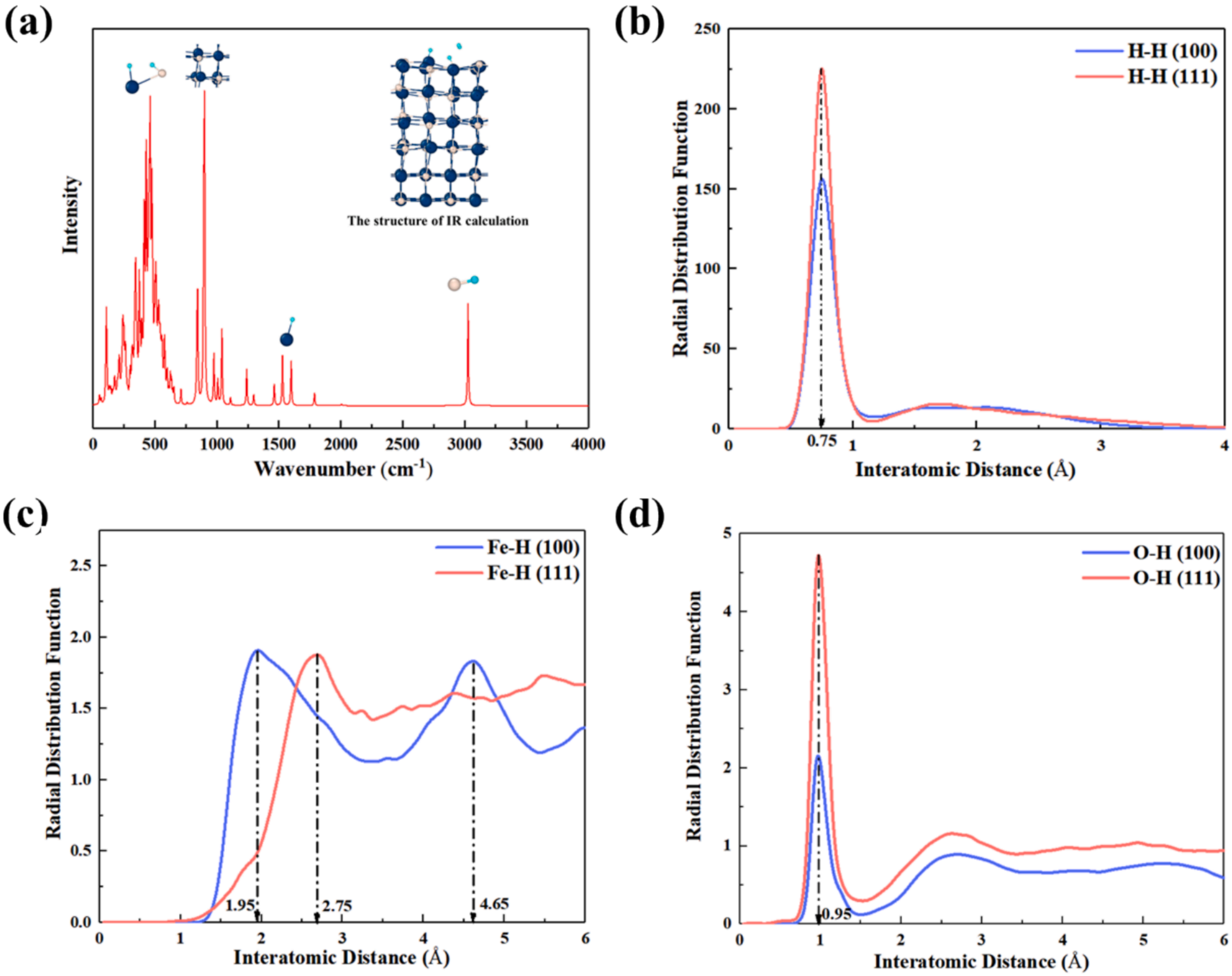

Fig. 6. The spectroscopy and structural analysis of FeO-H_2 reduction model. (a) The calculated IR spectra for the interaction between FeO and H_2. (b) The radial distribution function between H atoms. (c) The radial distribution function between the Fe and the H atom. (d) The radial distribution function between O atom and H atom.

(2,1) structure proceed more readily. Increasing the number of H_2 molecules, and consequently the number of adsorbed H atoms on the surface, destabilizes the surface structure. This effect, in turn, enhances the easier migration of H atoms and promotes the formation of H_2O molecules.

5. Conclusions

In summary, the underlying atomistic mechanisms of H_2 reducing O atoms from the surfaces of FeO(1 0 0) and FeO(1 1 1)$_{\text{O-terminated}}$ have been explored through *ab initio* meta-dynamics simulation. Our study reveals that the H_2 reduction process comprises two distinct reaction stages, each governed by a critical rate-limiting step. The formation of O–H bonds and the breaking of O-Fe bonds occur via different mechanisms. The FeO crystal serves as a catalyst, reducing the energy barrier for H_2 dissociation and thereby enhancing the likelihood of the reaction. Additionally, we validated the reliability of the simulated reaction structures through IR spectroscopy analysis. These findings offer new basic insights into the reduction mechanisms in hydrogen-based sustainable metallurgy and provide valuable guidance for predicting and optimizing reaction efficiency of corresponding reactors.

CRediT authorship contribution statement

Chunhe Jiang: Writing – original draft, Investigation, Data curation, Conceptualization. **Kejiang Li:** Writing – review & editing, Supervision, Investigation, Conceptualization. **Jianliang Zhang:** Supervision, Funding acquisition. **Yan Ma:** Writing – review & editing.

Declaration of competing interest

The authors declare that they have no known competing financial interests or personal relationships that could have appeared to influence the work reported in this paper.

Acknowledgments

The authors acknowledge the support of the National Science Foundation of China (52404336), China Postdoctoral Science Foundation (2024M750176), Postdoctoral Fellowship Program of CPSF (GZC20240109), and the Young Elite Scientist Sponsorship Program by CAST (YESS20210090). The authors acknowledge the many highly valuable and intense scientific discussions with Dierk Raabe from the Max Planck Institute for Sustainable Materials (MPI-SusMat).

Appendix A. Supplementary data

Supplementary data to this article can be found online at https://doi.org/10.1016/j.apsusc.2025.163031.

Data availability

Data will be made available on request.

References

[1] S. Pauliuk, T. Wang, D.B. Müller, Steel all over the world: Estimating in-use stocks of iron for 200 countries, Resour. Conserv. Recycl. 71 (2013) 22–30.

[2] T. Lei, D. Wang, X. Yu, S. Ma, W. Zhao, C. Cui, J. Meng, S. Tao, D. Guan, Global iron and steel plant CO2 emissions and carbon-neutrality pathways, Nature (2023) 1–7.

[3] L. Hermwille, S. Lechtenböhmer, M. Åhman, H. van Asselt, C. Bataille, S. Kronshage, A. Tönjes, M. Fischedick, S. Oberthür, A. Garg, A climate club to decarbonize the global steel industry, Nat. Clim. Chang. 12 (2022) 494–496.

[4] A.N. Conejo, J.-P. Birat, A. Dutta, A review of the current environmental challenges of the steel industry and its value chain, J. Environ. Manage. 259 (2020) 109782.

[5] L. Ren, S. Zhou, T. Peng, X. Ou, A review of CO2 emissions reduction technologies and low-carbon development in the iron and steel industry focusing on China, Renew. Sustain. Energy Rev. 143 (2021) 110846.

[6] F. Patisson, O. Mirgaux, Hydrogen ironmaking: How it works, Metals 10 (2020) 922.

[7] K. Ma, J. Deng, G. Wang, Q. Zhou, J. Xu, Utilization and impacts of hydrogen in the ironmaking processes: a review from lab-scale basics to industrial practices, Int. J. Hydrogen Energy 46 (2021) 26646–26664.

[8] I.R. Souza Filho, H. Springer, Y. Ma, A. Mahajan, C.C. da Silva, M. Kulse, D. Raabe, Green steel at its crossroads: Hybrid hydrogen-based reduction of iron ores, J. Clean. Prod. 340 (2022) 130805.

[9] Y. Chen, H. Zuo, Review of hydrogen-rich ironmaking technology in blast furnace, Ironmak. Steelmak. 48 (2021) 749–768.

[10] R. Wang, Y. Zhao, A. Babich, D. Senk, X. Fan, Hydrogen direct reduction (H-DR) in steel industry—An overview of challenges and opportunities, J. Clean. Prod. 329 (2021) 129797.

[11] P. Behera, B. Bhoi, R. Paramguru, P. Mukherjee, B. Mishra, Hydrogen plasma smelting reduction of Fe 2 O 3, Metall. Mater. Trans. B 50 (2019) 262–270.

[12] M. Jovičević-Klug, I.R. Souza Filho, H. Springer, C. Adam, D. Raabe, Green steel from red mud through climate-neutral hydrogen plasma reduction, Nature 625 (2024) 703–709.

[13] I.R. Souza Filho, Y. Ma, M. Kulse, D. Ponge, B. Gault, H. Springer, D. Raabe, Sustainable steel through hydrogen plasma reduction of iron ore: Process, kinetics, microstructure, chemistry, Acta Mater. 213 (2021) 116971.

[14] H. Pauna, D. Ernst, M. Zarl, I.R.d. Souza Filho, M. Kulse, Ö. Büyükuslu, M. Jovičević-Klug, H. Springer, M. Huttula, J. Schenk, The Optical Spectra of Hydrogen Plasma Smelting Reduction of Iron Ore: Application and Requirements, steel research international, (2024) 2400028.

[15] M.-F. Rau, D. Rieck, J.W. Evans, Investigation of iron oxide reduction by TEM, Metall. Trans. B 18 (1987) 257–278.

[16] Q. Tsay, W. Ray, J. Szekely, The modeling of hematite reduction with hydrogen plus carbon monoxide mixtures: Part II. The direct reduction process in a shaft furnace arrangement, AIChE J. 22 (1976) 1072–1079.

[17] Y. Ma, I.R. Souza Filho, Y. Bai, J. Schenk, F. Patisson, A. Beck, J.A. van Bokhoven, M.G. Willinger, K. Li, D. Xie, Hierarchical nature of hydrogen-based direct reduction of iron oxides, Scripta Materialia, 213 (2022) 114571.

[18] Y. Bai, J.R. Mianroodi, Y. Ma, A.K. da Silva, B. Svendsen, D. Raabe, Chemo-mechanical phase-field modeling of iron oxide reduction with hydrogen, Acta Mater. 231 (2022) 117899.

[19] M. Pei, M. Petäjäniemi, A. Regnell, O. Wijk, Toward a fossil free future with HYBRIT: Development of iron and steelmaking technology in Sweden and Finland, Metals 10 (2020) 972.

[20] U. Herrmann, N. Pieton, B. Pfluger, K. Alms, T.M. Kneiske, C. Voglstätter, B. Klaassen, R. Burlacu, A. Martin, B.O. Gerloff, Hydrogen infrastructures—Networks and storage, in: Hydrogen Technologies, Springer, 2022, pp. 171-202.

[21] I.R. Souza Filho, Y. Ma, D. Raabe, H. Springer, Fundamentals of green steel production: on the role of gas pressure during hydrogen reduction of iron ores, JOM 75 (2023) 2274–2286.

[22] Ö. Özgün, I. Dirba, O. Gutfleisch, Y. Ma, D. Raabe, Green ironmaking at higher H2 pressure: reduction kinetics and microstructure formation during hydrogen-based direct reduction of hematite pellets, J. Sustain. Metall. (2024) 1–14.

[23] A. Pineau, N. Kanari, I. Gaballah, Kinetics of reduction of iron oxides by H2: Part I: Low temperature reduction of hematite, Thermochim Acta 447 (2006) 89–100.

[24] A. Pineau, N. Kanari, I. Gaballah, Kinetics of reduction of iron oxides by H2: Part II. Low temperature reduction of magnetite, Thermochimica Acta 456 (2007) 75–88.

[25] C. McCammon, L.-G. Liu, The effects of pressure and temperature on nonstoichiometric wüstite, Fe x O: the iron-rich phase boundary, Phys. Chem. Miner. 10 (1984) 106–113.

[26] S. Chen, J. Zhang, Y. Wang, T. Wang, Y. Li, Z. Liu, Thermodynamic study of H2-FeO based on the principle of minimum Gibbs free energy, Metals 13 (2023) 225.

[27] S. Li, H. Gu, A. Huang, Y. Zou, S. Yang, L. Fu, Thermodynamic analysis and experimental verification of the direct reduction of iron ores with hydrogen at elevated temperature, J. Mater. Sci. 57 (2022) 20419–20434.

[28] H.-B. Zuo, C. Wang, J.-J. Dong, K.-X. Jiao, R.-S. Xu, Reduction kinetics of iron oxide pellets with H 2 and CO mixtures, Int. J. Miner. Metall. Mater. 22 (2015) 688–696.

[29] A. El-Geassy, M. Nasr, Influence of the original structure on the kinetics of hydrogen reduction of hematite compacts, Trans. Iron Steel Institute Japan 28 (1988) 650–658.

[30] M. Bahgat, M. Khedr, Reduction kinetics, magnetic behavior and morphological changes during reduction of magnetite single crystal, Mater. Sci. Eng. B 138 (2007) 251–258.

[31] N. Thüns, B. Krooss, Q. Zhang, H. Stanjek, The effect of H2 pressure on the reduction kinetics of hematite at low temperatures, Int. J. Hydrogen Energy 44 (2019) 27615–27625.

[32] E. Aa, V. Rajakumar, Gaseous reduction of wustite with H2, CO and H2-CO mixtures, Trans. Iron Steel Institute Japan 25 (1985) 449–458.

[33] K. Piotrowski, K. Mondal, H. Lorethova, L. Stonawski, T. Szymański, T. Wiltowski, Effect of gas composition on the kinetics of iron oxide reduction in a hydrogen production process, Int. J. Hydrogen Energy 30 (2005) 1543–1554.

[34] D. Spreitzer, J. Schenk, Reduction of iron oxides with hydrogen—a review, Steel Res. Int. 90 (2019) 1900108.

[35] Ö. Özgün, X. Lu, Y. Ma, D. Raabe, How much hydrogen is in green steel? npj Mater. Degrad. 7 (2023) 78.

[36] X. Zhou, Y. Bai, A.A. El-Zoka, S.-H. Kim, Y. Ma, C.H. Liebscher, B. Gault, J. R. Mianroodi, G. Dehm, D. Raabe, Effect of pore formation on redox-driven phase transformation, Phys. Rev. Lett. 130 (2023) 168001.

[37] A.A. El-Zoka, L.T. Stephenson, S.H. Kim, B. Gault, D. Raabe, The Fate of Water in Hydrogen-Based Iron Oxide Reduction, Adv. Sci. 10 (2023) 2300626.

[38] X. Zheng, S. Paul, L. Moghimi, Y. Wang, R.A. Vilá, F. Zhang, X. Gao, J. Deng, Y. Jiang, X. Xiao, Correlating chemistry and mass transport in sustainable iron production, Proc. Natl. Acad. Sci., 120 (2023) e2305097120.

[39] Q. Tang, K. Huang, Determining the kinetic rate constants of Fe3O4-to-Fe and FeO-to-Fe reduction by H2, Chem. Eng. J. 434 (2022) 134771.

[40] W. Jozwiak, E. Kaczmarek, T. Maniecki, W. Ignaczak, W. Maniukiewicz, Reduction behavior of iron oxides in hydrogen and carbon monoxide atmospheres, Appl. Catal. A 326 (2007) 17–27.

[41] A.-H.A. El-Geassy, Rate controlling step in the reduction of iron oxides; kinetics and mechanism of wüstite-iron step in H2, CO and H2/CO gas mixtures, in: IOP Conference Series: Materials Science and Engineering, IOP Publishing, 2017, pp. 012002.

[42] K. Salah Uddin, B. Middendorf, Reactivity of different crystalline surfaces of C3S during early hydration by the atomistic approach, Materials 12 (2019) 1514.

[43] Y. Li, H. Pan, Q. Liu, X. Ming, Z. Li, Ab initio mechanism revealing for tricalcium silicate dissolution, Nat. Commun. 13 (2022) 1253.

[44] L.G. Wade, Organic chemistry, Pearson Education India, 2008.

[45] L. Zhang, M. Zhou, L. Shao, W. Wang, K. Fan, Q. Qin, Reactions of Fe with H2O and FeO with H2. A combined matrix isolation FTIR and theoretical study, J. Phys. Chem. A 105 (2001) 6998–7003.

[46] J. Hutter, M. Iannuzzi, F. Schiffmann, J. VandeVondele, cp2k: atomistic simulations of condensed matter systems, Wiley Interdiscip. Rev.: Comput. Mol. Sci. 4 (2014) 15–25.

[47] J. VandeVondele, M. Krack, F. Mohamed, M. Parrinello, T. Chassaing, J. Hutter, Quickstep: Fast and accurate density functional calculations using a mixed Gaussian and plane waves approach, Comput. Phys. Commun. 167 (2005) 103–128.

[48] S. Goedecker, M. Teter, J. Hutter, Separable dual-space Gaussian pseudopotentials, Phys. Rev. B 54 (1996) 1703.

[49] C. Hartwigsen, S. Gœdecker, J. Hutter, Relativistic separable dual-space Gaussian pseudopotentials from H to Rn, Phys. Rev. B 58 (1998) 3641.

[50] J. VandeVondele, J. Hutter, Gaussian basis sets for accurate calculations on molecular systems in gas and condensed phases, J. Chem. Phys. 127 (2007).

[51] J.P. Perdew, K. Burke, M. Ernzerhof, Generalized gradient approximation made simple, Phys. Rev. Lett. 77 (1996) 3865.

[52] S. Grimme, J. Antony, S. Ehrlich, H. Krieg, A consistent and accurate ab initio parametrization of density functional dispersion correction (DFT-D) for the 94 elements H-Pu, J. Chem. Phys. 132 (2010).

[53] D.J. Evans, B.L. Holian, The nose–hoover thermostat, J. Chem. Phys. 83 (1985) 4069–4074.

[54] M. Yu, S. Yang, C. Wu, N. Marom, Machine learning the Hubbard U parameter in DFT+ U using Bayesian optimization, npj computational materials, 6 (2020) 180.

[55] G. Rollmann, A. Rohrbach, P. Entel, J. Hafner, First-principles calculation of the structure and magnetic phases of hematite, Phys. Rev. B 69 (2004) 165107.

[56] A. Kéri, R. Dähn, M. Krack, S.V. Churakov, Combined XAFS spectroscopy and ab initio study on the characterization of iron incorporation by montmorillonite, Environ. Sci. Tech. 51 (2017) 10585–10594.

[57] A. Liechtenstein, V.I. Anisimov, J. Zaanen, Density-functional theory and strong interactions: orbital ordering in Mott-Hubbard insulators, Phys. Rev. B 52 (1995) R5467.

[58] S.L. Dudarev, G.A. Botton, S.Y. Savrasov, C. Humphreys, A.P. Sutton, Electron-energy-loss spectra and the structural stability of nickel oxide: An LSDA+ U study, Phys. Rev. B 57 (1998) 1505.

[59] S. Zhang, K. Li, Y. Ma, Y. Bu, Z. Liang, Z. Yang, J. Zhang, The adsorption mechanism of hydrogen on FeO crystal surfaces: a density functional theory study, Nanomaterials 13 (2023) 2051.

[60] R. Ashraf, S. Riaz, M.S. Akhtar, S. Naseem, Study of structural and electronic properties of iron oxide by ADF, in: Proc. The 2014 World Congress on Advances in Civil, Environmental and Materials Research (ACEM'14), 2014.

[61] P. Battle, A. Cheetham, The magnetic structure of non-stoichiometric ferrous oxide, J. Phys. C Solid State Phys. 12 (1979) 337.

[62] U.D. Wdowik, P. Piekarz, K. Parlinski, A.M. Oleś, J. Korecki, Strong effects of cation vacancies on the electronic and dynamical properties of FeO, Physical Review B—Condensed Matter and Materials, Physics 87 (2013) 121106.

[63] Y. Meng, X.-W. Liu, C.-F. Huo, W.-P. Guo, D.-B. Cao, Q. Peng, A. Dearden, X. Gonze, Y. Yang, J. Wang, When density functional approximations meet iron oxides, J. Chem. Theory Comput. 12 (2016) 5132–5144.

[64] I. Bernal-Villamil, S. Gallego, Electronic structure and polaronic charge distributions of Fe vacancy clusters in Fe 1− x O, Physical Review B, 90 (2014) 195126.

[65] M. Bonomi, D. Branduardi, G. Bussi, C. Camilloni, D. Provasi, P. Raiteri, D. Donadio, F. Marinelli, F. Pietrucci, R.A. Broglia, PLUMED: A portable plugin for free-energy calculations with molecular dynamics, Comput. Phys. Commun. 180 (2009) 1961–1972.

[66] G.A. Tribello, M. Bonomi, D. Branduardi, C. Camilloni, G. Bussi, PLUMED 2: New feathers for an old bird, Comput. Phys. Commun. 185 (2014) 604–613.

[67] T. Lu, F. Chen, Multiwfn: a multifunctional wavefunction analyzer, J. Comput. Chem. 33 (2012) 580–592.

[68] H. Zhong, L. Wen, J. Li, J. Xu, M. Hu, Z. Yang, The adsorption behaviors of CO and H2 on FeO surface: A density functional theory study, Powder Technol. 303 (2016) 100–108.

[69] K.-P. Huber, Molecular spectra and molecular structure: IV, Springer Science & Business Media, Constants of diatomic molecules, 2013.

[70] R. Ditchfield, Theoretical studies of magnetic shielding in H2O and (H2O) 2, J. Chem. Phys. 65 (1976) 3123–3133.